Decorrelating Ambiguities in SAR Interferometry Through Slight PRI Variation

Michelangelo Villano, *Senior Member, IEEE*, Maxwell Nogueira Peixoto, Nertjana Ustalli, *Member, IEEE*, Josef Mittermayer, Gerhard Krieger, *Fellow, IEEE*, and Alberto Moreira, *Fellow, IEEE*

***Abstract*— Synthetic aperture radar (SAR) interferometry is a well-established technique for producing high-resolution digital elevation models (DEMs) of the Earth's surface and measuring displacements on different time scales. Observations of SAR interferograms, however, show that azimuth ambiguities can be coherently imaged and may lead to phase biases and coherence losses that significantly degrade the interferometric performance. Whereas imposing very low ambiguity levels may represent a severe design constraint for a spaceborne SAR system, a slight variation of the pulse repetition interval (PRI) is a new, simple, yet effective technique to decorrelate ambiguities, which, in turn, reduces the phase biases and coherence losses without substantially affecting the imaged swath width. An additional benefit of the PRI variation is that range ambiguities also become decorrelated. This article addresses two cases. For the repeat-pass case, slightly different pulse repetition frequencies (PRFs) can be used for the two acquisitions, and the minimum required PRF difference can be analytically derived resorting to the power spectral density of the ambiguous signals. For the single-pass case, a slight variation of the PRI during the common acquisition is an effective solution in case an along-track baseline is present. In particular, a square wave PRI variation scheme outperforms sinusoidal or random ones. Finally, simulations using TanDEM-X data are presented to show the improvement in interferogram and DEM quality resulting from ambiguity decorrelation. This work is relevant for the design of future spaceborne interferometric SAR systems and for the enhanced exploitation of current ones.**

***Index Terms*— Azimuth ambiguities, interferometry, microwave remote sensing, synthetic aperture radar (SAR).**

I. Introduction

SYNTHETIC aperture radar (SAR) interferometry exploits the coherent combination of two or more SAR images for a large number of applications. If two images, often referred to as the master and slave images, are acquired from slightly different viewing angles, a digital elevation model (DEM) of the observed scene can be formed, while images acquired at different times from the same position allow for measurements of, e.g., ocean current velocity using along-track SAR interferometry or radial displacements using differential interferometry [1], [2], [3], [4]. The accuracy of the resulting products ultimately depends on the complex correlation (or coherence) between the two SAR images, which is the product of the contributions of various decorrelation sources, such as thermal noise, quantization noise, baseline decorrelation, volume decorrelation, Doppler decorrelation, temporal decorrelation, coregistration and processing errors, and range and azimuth ambiguities [5], [6].

Azimuth ambiguities were initially accounted for through a decorrelation contribution $\gamma_{\text{amb,az}}$ given by

$$\gamma_{\text{amb,az}} = 1/(1 + \text{AASR}) \tag{1}$$

where AASR is the azimuth ambiguity-to-signal ratio, i.e., in a similar way as thermal noise [7], [8]. Observations of several TanDEM-X interferograms, such as the one in Fig. 1 acquired over the Franz Josef Land, Russia, however, have shown that azimuth ambiguities may be coherently imaged and lead to significant interferometric phase biases φ_{bias} and modulations of the coherence magnitude γ, which can be analytically described by the following expressions, derived in [9] (2) and (3), as shown at the bottom of the next page, where $\text{AASR}_{\text{local}}$ is the local AASR, γ_m and $\varphi_{o,m}$ are the coherence magnitude and interferometric phase of the ambiguity-free interferogram, respectively, and γ_a and $\varphi_{o,a}$ are the coherence magnitude and the interferometric phase of the interferogram of the ambiguities, respectively.

A spectral-based technique to estimate the local AASR is presented in [10], where it is also shown that the latter ratio is likely to be larger than -10 dB in low-backscatter areas and can even reach 0 dB in some cases. As discussed in [11], a local AASR of -5 dB results in a phase bias characterized by a standard deviation of 5°–10° (depending on the signal-to-noise ratio) and a decorrelation contribution due to azimuth ambiguities in the order of 0.7–0.8. The aforementioned decorrelation and phase bias contributions are critical to be accounted for in the overall height error and coherence budget. One could reduce the local AASR by imposing a lower AASR requirement in the overall design, but this would drive the complexity and the cost of the SAR system, e.g., by increasing the length of the azimuth antenna and introducing a weighting in the azimuth antenna to decrease the sidelobes. Please note that a simple increase in the PRF leads to a decrease in the swath width in order to keep the range ambiguities at an acceptable level.

The local ambiguity-to-signal ratio could also be reduced by removing azimuth ambiguities through a postprocessing step [12], [13], [14], [15], [16], [17], [18], [19]. A Wiener filter could be applied, as proposed in [13], but this would

Manuscript received 4 July 2022; revised 18 October 2022; accepted 29 November 2022. Date of publication 7 December 2022; date of current version 20 December 2022. *(Corresponding author: Michelangelo Villano.)*

The authors are with the Microwaves and Radar Institute, German Aerospace Center (DLR), 82234 Weßling, Germany (e-mail: michelangelo.villano@dlr.de).

Digital Object Identifier 10.1109/TGRS.2022.3227316

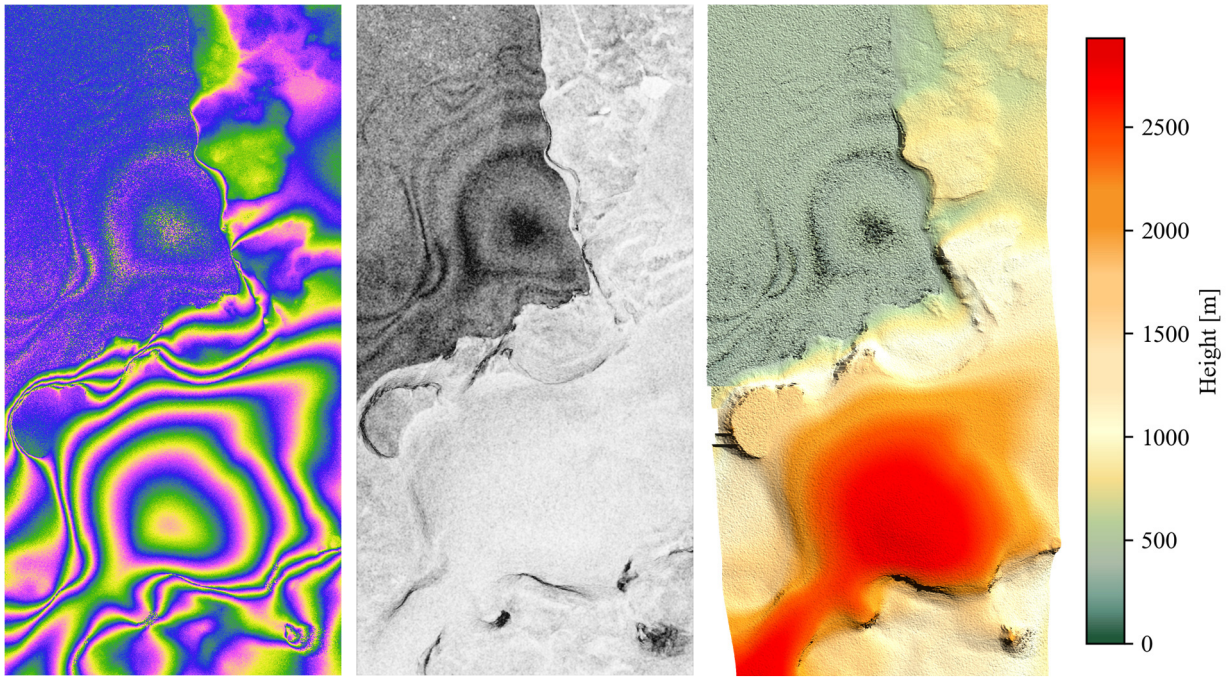

Fig. 1. (Left) Interferometric phase, (center) magnitude of the complex coherence, and (right) DEM of a detail of a TanDEM-X interferogram affected by azimuth ambiguities, acquired over the Franz Josef Land, Russia. The horizontal and vertical axes represent the ground range (5.12 km) and azimuth (10.24 km), respectively. The azimuth ambiguities of the mountain in the lower part of the image are seen in the upper part as a bias in the sea ice region.

result in a resolution degradation, which turns into a reduction of the number of interferometric looks and, thus, into a lower coherence. Ambiguities could also be coherently subtracted directly from the interferogram, as was first demonstrated in 2011 in a DLR-internal study to reduce the phase errors and coherence losses in the TanDEM-X interferogram of Fig. 1 (see [9] and [11]). This technique was then further elaborated for short-baseline along-track interferometry in [20] and [21], but the accurate and fully autonomous estimation of the complex scaling coefficient makes this technique challenging.

Equations (2) and (3) suggest that the phase bias and the coherence loss can also be controlled by limiting the coherence magnitude of the interferogram of the ambiguities γ_a, i.e., by decorrelating the azimuth ambiguities of the master and slave images. If total decorrelation is achieved, there is no interferometric phase bias anymore, and the decorrelation contribution degenerates into the expression in (1), where AASR has still to be understood as the local one, i.e., the decorrelation contribution due to azimuth ambiguities is similar to the one due to thermal noise.

γ_a is influenced by the acquisition geometry, which, in some cases, makes the azimuth ambiguities of the master and slave images mutually shifted and, therefore, decorrelated. Under the conservative assumption that the acquisition geometry leads to full overlap of the ambiguities, ambiguity decorrelation can still be achieved by acting on the mutual sampling of the master and slave images.

This article is organized as follows. Section II addresses the repeat-pass case, for which an analytical expression of the minimum required pulse repetition frequency (PRF) difference between the two acquisitions is derived. Section III considers, instead, the single-pass case and presents different pulse repetition interval (PRI) variation schemes together with the resulting swath width reduction and ambiguity decorrelation. In Section IV, the impact of ambiguity decorrelation on interferogram and DEM quality is assessed through simulations using TanDEM-X data. Conclusions are drawn in Section V.

II. Repeat-Pass SAR Interferometry

If the master and slave images are acquired at different times, the adoption of slightly different PRFs in the two acquisitions might suffice to decorrelate azimuth ambiguities. This case also includes the pursuit monostatic mode of TanDEM-X [6], where the time lag between the two acquisitions is in the order of a few seconds.

The minimum PRF difference ΔPRF required for decorrelation can be obtained by imposing that the relative azimuth shift Δx of the first-order azimuth ambiguities between the

$$\varphi_{\text{bias}} = \arg\left\{1 + \text{AASR}_{\text{local}} \frac{\gamma_a}{\gamma_m} e^{j(\varphi_{0,a} - \varphi_{o,m})}\right\} \tag{2}$$

$$\gamma = \frac{1}{1 + \text{AASR}_{\text{local}}} \cdot \sqrt{\gamma_m^2 + \text{AASR}_{\text{local}}^2 \gamma_a^2 + 2\text{AASR}_{\text{local}} \frac{\gamma_a}{\gamma_m} \cos\left(\varphi_{0,a} - \varphi_{o,m}\right)} \tag{3}$$

two acquisitions is larger than the autocorrelation length ℓ_a of the ambiguous signals times the satellite speed.

The azimuth shift Δx is given by [22], [23], [24]

$$\Delta x = \frac{\lambda R_0 \Delta \mathrm{PRF}}{2 v_S} \tag{4}$$

where λ is the wavelength, R_0 is the radar-target range of the closest approach, and v_S is the satellite speed, whereas the autocorrelation length ℓ_a of the ambiguous signals depends on the power spectral density (PSD) of the ambiguous signals, therefore, on both the azimuth antenna pattern and the selected PRF. Fig. 2 shows the PSDs of the main signal and the first-order left ambiguity for TanDEM-X, which is characterized by a rectangular antenna with length $L = 4.8$ m and $\lambda = 0.03$ m, with PRF $= 3000$ Hz. It also provides the corresponding normalized autocorrelation functions, obtained as inverse Fourier transforms of the PSDs. Although, strictly speaking, the PSD and the autocorrelation function are different for the two ambiguous signals due to the different PRFs, a difference in the order of few Hz can be neglected. As is apparent, due to the shape of the PSD of the ambiguous signals, the autocorrelation length of the ambiguous signals can be several times (i.e., in this example, about five times) larger than that of the main signal, which is approximately equal to $L/(2v_S)$, i.e., 0.3 ms. The autocorrelation length becomes smaller for higher PRFs, i.e., around 5000 Hz, which are, however, unlikely to be used within typical TanDEM-X acquisitions.

Defining as α the ratio of the autocorrelation lengths of the ambiguous and main signals, it holds

$$\Delta \mathrm{PRF} > \alpha \frac{L v_S}{\lambda R_0} \tag{5}$$

where conservative values of α of at least 5 should be assumed. In other words, due to the shape of the PSD of the ambiguous signals, the minimum required PRF difference is such that it mutually shifts the first-order azimuth ambiguities by five azimuth resolution cells. For higher order azimuth ambiguities, the azimuth shift will be larger by a factor k equal to the order of the ambiguity, while the autocorrelation length of the ambiguous signal will be in the worst case and for a rectangular antenna in the same order of magnitude as the one obtained for first-order ambiguities.

For TanDEM-X, a ΔPRF $\cong$ 8 Hz is required for a PRF $\cong$ 3000 Hz, which does not significantly influence the width of the common swath to be imaged. As is apparent from its derivation, this simple model does not account for the defocusing of azimuth ambiguities resulting from the wrongly compensated range cell migration. However, 2-D simulations show that (5) still provides a good estimate of the ΔPRF value required for ambiguity decorrelation. The simulations are carried out by convolving the 2-D impulse responses of the system with complex white Gaussian signals representing distributed targets (fully developed speckle) and then estimating the coherence of the first-order azimuth ambiguities of the master and slave images as a function of the PRF difference ΔPRF. Fig. 3 shows the coherence of the first-order azimuth ambiguities as a function of ΔPRF obtained from

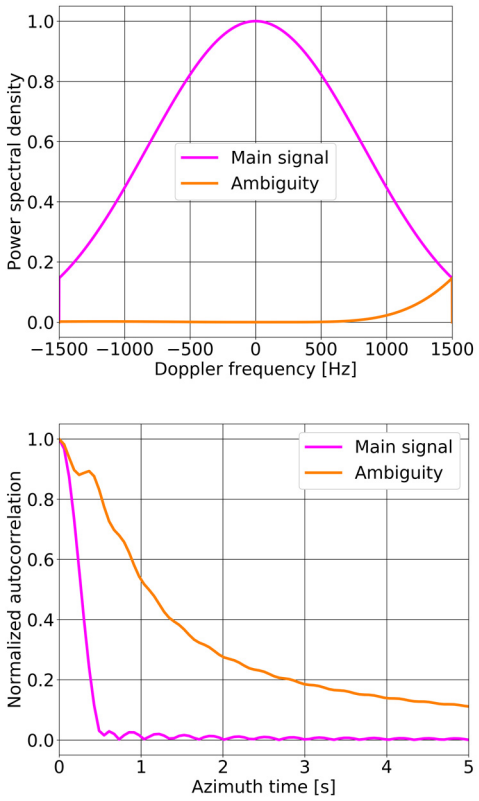

Fig. 2. Power spectral densities normalized to the maximum of (top) main signal and (bottom) normalized autocorrelation functions of the main signal and the first-order left ambiguity for TanDEM-X with PRF = 3000 Hz.

2-D simulations for TanDEM-X with a PRF $= 3000$ Hz (the coherence reduces significantly at ΔPRF $\cong$ 8 Hz, as expected), for a high-resolution X-band system with a 2.4-m-long antenna and a chirp bandwidth $B_r = 600$ MHz, and for an L-band system with a 10-m-long antenna. In all cases, there is full agreement with the estimates obtained using (5).

Note that, for the TanDEM-X case, the minimum value of ΔPRF obtained using (5) is smaller than the PRF difference $\Delta \mathrm{PRF}_{\text{no overlap}}$ required to avoid overlapping of the first-order azimuth ambiguities of the master and slave images, which is a sufficient condition for ambiguity decorrelation. $\Delta \mathrm{PRF}_{\text{no overlap}}$ can be obtained by imposing that the azimuth shift Δx is larger than the azimuth extension of the first-order azimuth ambiguities (in meters) E_a, which, accounting for the defocusing due to the wrongly compensated range-cell migration, is given by [22], [23], [24]

$$E_a \cong \frac{\mathrm{PRF} \lambda^2 R_0}{4 v_S \delta_r} \tag{6}$$

where δ_r is the range resolution of the system. It holds

$$\Delta \mathrm{PRF}_{\text{no overlap}} > \frac{\lambda \mathrm{PRF}}{2 \delta_r}. \tag{7}$$

For a TanDEM-X acquisition with $B_r = 100$ MHz, a PRF difference in the order of $\Delta \mathrm{PRF}_{\text{no overlap}} \cong 30$ Hz for PRF $\cong$ 3000 Hz is required to avoid overlap of the first-order azimuth ambiguities, i.e., larger than the PRF difference required for

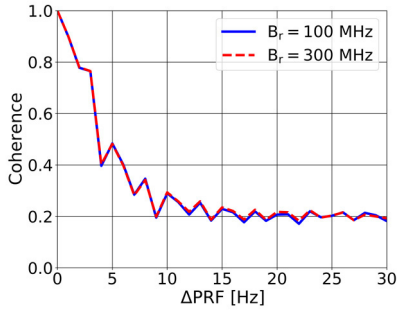

(a)

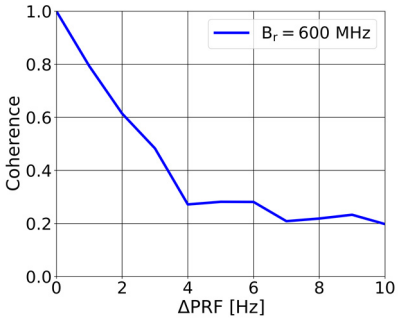

(b)

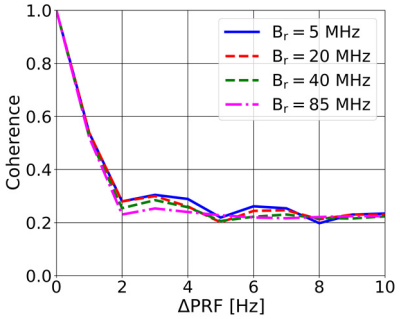

(c)

Fig. 3. Coherence of the ambiguities for repeat-pass SAR interferometry as a function of the PRF difference between the two acquisitions ΔPRF for (a) TanDEM-X with PRF = 3000 Hz, (b) high-resolution X-band system with a 2.4-m-long antenna, and (c) L-band system with a 10-m-long antenna and different values of the chirp bandwidth B_r.

ambiguity decorrelation. This means that azimuth ambiguities can be decorrelated, even if they partially overlap.

Furthermore, as a consequence of the use of different PRFs, range ambiguities of the master and slave images will also be relatively displaced in range and will not overlap nor produce any coherent interference, as long as

$$\left|\frac{1}{\mathrm{PRF}+\Delta\mathrm{PRF}}-\frac{1}{\mathrm{PRF}}\right|\frac{c_0}{2}\cong\frac{\Delta\mathrm{PRF}}{\mathrm{PRF}^2}\frac{c_0}{2}>\delta_r \tag{8}$$

where c_0 is the speed of light and where it has been assumed that the first-order range ambiguity is only smeared in azimuth (due to the mismatch in the azimuth compression) and not in the range direction [22]. For the TanDEM-X example, where the minimum required PRF difference to achieve ambiguity decorrelation was calculated to be ΔPRF ≅ 8 Hz for PRF = 3000 Hz, (8) is already verified for slant range resolutions

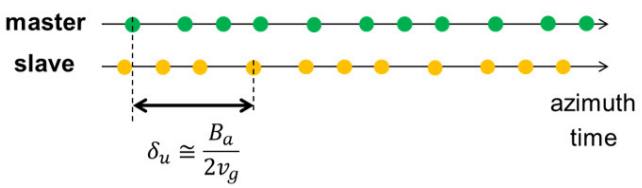

Fig. 4. Relative azimuth time shift of the samples after co-registration resulting from a nonzero along-track baseline.

better than 133.2 m, i.e., the slight PRF difference has the additional benefit of mutually shifting range ambiguities of the master and slave images and preventing any coherent interference of range ambiguities.

If a large interferometric stack has to be created, the selection of numerous distinct PRFs, which lead to mutually decorrelated ambiguities, is constrained by the timing (or diamond) diagram. Those constraints can be relaxed by adopting techniques based on waveform variation and dual-focus postprocessing that help the system designer get rid of the nadir interference [25], [26]. For example, in the presence of the sole transmit interference, for TanDEM-X and a ground swath width of 30 km, a PRF span ranging from about 50 (far range) to about 100 Hz (near range) is available around PRF = 3200 Hz. This means that, assuming a total decorrelation for ΔPRF ≅ 8 Hz, a number of distinct PRFs ranging from 7 (far range) to 13 (near range) can be used. If a larger number of distinct PRFs is needed, a significant ambiguity decorrelation is still obtained for smaller PRF spacing, e.g., the coherence drops to around 0.4 for ΔPRF ≅ 4 Hz in the TanDEM-X example of Fig. 3(a). Moreover, the residual phase biases of different interferograms within the stack will be randomly distributed with a mean interferometric phase equal to zero; therefore, the resulting phase bias for an image stack will depend on the overall processing and is likely to become successively smaller, as more and more datasets are combined.

III. Single-Pass SAR Interferometry

If the master and slave images are acquired at the same time and a single transmitter is used, the adoption of a slight PRI variation during the acquisition could help decorrelate ambiguities, as long as a nonzero along-track baseline B_a is present. The impulse response function (IRF) in the proximity of the ambiguities, in fact, is azimuth-variant in the case of variable PRI, and the along-track baseline induces (after coregistration) a relative azimuth time shift δ_u between the available azimuth samples of the master and slave images roughly given by

$$\delta_u \cong \frac{B_a}{2v_g} \tag{9}$$

where v_g is the ground velocity and a bistatic configuration has been assumed with the same satellite transmitting all pulses (see Fig. 4).

Under the assumption that the acquisition geometry leads to overlap of the ambiguities, the absence of an along-track

baseline leads to the same IRFs for the master and slave image independently of the PRI variation scheme. At the same time, the presence of an along-track baseline without a PRI variation is not sufficient to avoid correlation of the ambiguities, as the ambiguities of the master and slave images might be characterized by different phases, but their phase difference would still be constant (the latter is also the case in Fig. 1).

In the presence of the aforementioned relative shift, the raw data of master and slave could be resampled, e.g., using best linear unbiased (BLU) interpolation [27], [28], [29], [30], to a uniform grid before focusing and interferogram formation. The coefficients of the BLU interpolation depend on the spectrum of the main signal and are not the optimal ones to resample the ambiguous signal, which has a different spectrum and will, therefore, be resampled in a wrong way and, in general, in a different way in the master and slave images, leading to a decorrelation of the ambiguities.

An additional advantage of a PRI variation, especially if followed by a "wrong" resampling, is that ambiguities will be further smeared compared to the constant PRF case and will be, therefore, characterized by a reduced range resolution. This corresponds to a smaller critical baseline for the ambiguities, which could, in turn, result in a decorrelation of the ambiguities of distributed scatterers.

A. PRI Variation Schemes

The PRI variation scheme will influence the positions of the blind ranges for each range line. In particular, the positions of the blind ranges depend on the moving sum of a number of consecutive PRIs equal to the number of traveling pulses n_t [32], which is roughly given by

$$n_t \cong \frac{2R_0}{c_0 \mathrm{PRI}_{\mathrm{mean}}} \tag{10}$$

where c_0 is the speed of light and $\mathrm{PRI}_{\mathrm{mean}}$ is the mean PRI.

The continuous variation of the PRI recalls that staggered SAR systems, which includes BLU interpolation as an integrating part of the concept [27], [28], [29], [30], are characterized by the smeared and decorrelated range and azimuth ambiguities [24], [32], and are well suited for interferometry [33], [34], [35]. While, in staggered SAR, however, a PRI variation is required, which ideally shifts blind ranges to all possible positions across the swath in order to have them uniformly distributed, for the scope of this work, the PRI variation should allow keeping the width of the imaged swath. Considering that, for most SAR systems, the imaged swath is smaller than the maximum one allowed by the timing (or diamond) diagram due to, e.g., signal-to-noise ratio or ambiguity requirements, and a small variation of the blind ranges across the synthetic aperture can be tolerated.

Three PRI variation schemes are considered in the following.

1) Sinusoidal PRI variation, whose PRIs can be written as

$$\mathrm{PRI}_k = \mathrm{PRI}_{\mathrm{mean}}\left(1 + A \sin\frac{2\pi k}{N}\right), \quad k = 0, \ldots, N-1 \tag{11}$$

where A is the amplitude of the PRI variation, e.g., $A = 0.01$ means that the PRI variation is $\pm 1\%$ with respect to $\mathrm{PRI}_{\mathrm{mean}}$, and N is the length (to be understood as the number of PRIs) of the sequence, which repeats then periodically.

1) Square wave PRI variation, whose PRIs can be written as

$$\mathrm{PRI}_k = \begin{cases} \mathrm{PRI}_{\mathrm{mean}}(1+A), & k = 0, \ldots, N/2-1 \\ \mathrm{PRI}_{\mathrm{mean}}(1-A), & k = N/2, \ldots, N-1 \end{cases} \tag{12}$$

with N even to keep the symmetry. In this case, only two distinct PRIs are used: the first PRI, $\mathrm{PRI}_{\mathrm{mean}}\ (1+A)$, is repeated $N/2$ times, then a second PRI, $\mathrm{PRI}_{\mathrm{mean}}\ (1-A)$, is repeated $N/2$ times, then the first PRI is repeated again $N/2$ times, and so on.

1) Random PRI variation (to be intended as a sequence of N random PRIs, which repeat periodically), whose PRIs can be written as

$$\mathrm{PRI}_k = \mathrm{PRI}_{\mathrm{mean}}[1 + A a_k], \quad k = 0, \ldots, N-1 \tag{13}$$

where a_k is an independent realization of a random variable with uniform distribution in the interval $[-1; 1]$. The advantage of repeating the same sequence of random realizations is justified in Section III-B.

Note that the three PRI variation schemes are expressed so that they are characterized by the same PRI span if the value of A is the same. Fig. 5 shows the PRI trend for two cycles of PRI variation for the three presented sequences with $\mathrm{PRI}_{\mathrm{mean}} = 0.303$ ms, $N = 100$, and $A = 0.007$.

B. Swath Reduction

If the length N of the sequence of PRIs is much larger than the number of traveling pulses n_t, the maximum achievable swath width W_S for a sinusoidal or a square wave PRI variation is approximately given by

$$W_S \cong (1 - 2A\ n_t) W_{S_{\mathrm{const}}} \tag{14}$$

where $W_{S_{\mathrm{const}}}$ is the maximum swath width obtained for a constant PRI equal to $\mathrm{PRI}_{\mathrm{mean}}$, e.g., for $n_t = 16$ and $A = 0.001$, the maximum swath width would reduce by 3.2%; hence, the need of keeping the amplitude A is very small. The formula is derived under the conservative assumption that the n_t PRIs adjacent to the maximum PRI are all equal to the maximum PRI.

Still, under the assumption that the length N of the PRI sequence of PRIs is much larger than the number of traveling pulses n_t, the assessment of the swath reduction for the periodic random PRI variation of (13) cannot be approximated in a straightforward way as in the case of sinusoidal and square wave PRI variations but requires some further considerations. Due to the randomness of the PRI, theoretically, the swath reduction could also reach the value provided in (14), but this worst case would only happen in the very unlikely case that n_t consecutive independent realizations of a_k are all equal or almost equal to 1 (or -1). A more reasonable approach is to

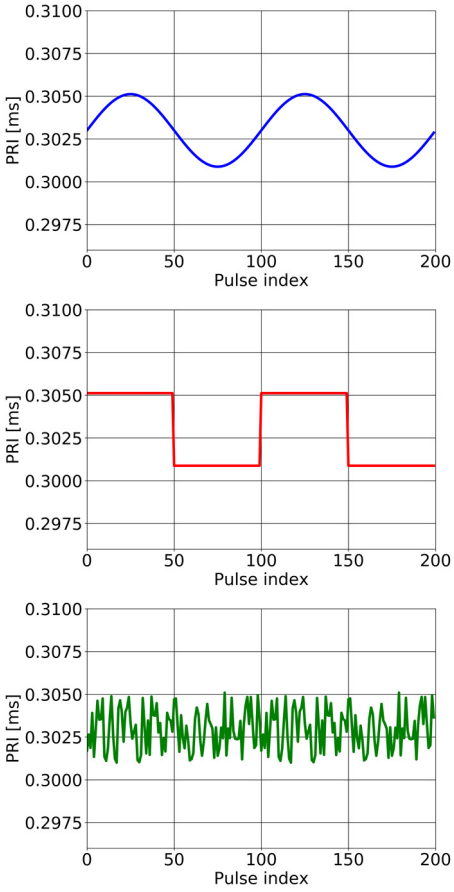

Fig. 5. (Top) Sinusoidal, (center) square wave, and (bottom) random PRI variation schemes provided in (11)–(13), respectively, for $\mathrm{PRI}_{\mathrm{mean}} = 0.303$ ms, $N = 100$, and $A = 0.007$. Two cycles are displayed.

resort to probability theory. The sum of n_t PRIs characterized as in (13), i.e., uniformly distributed, follows the Irwin–Hall distribution, which, for large values of n_t, can be approximated by a Gaussian distribution, whose standard deviation (relative to $\mathrm{PRI}_{\mathrm{mean}}$)$\sigma$ is given by $A(n)_t^{1/2}/(3)^{1/2}$. By considering an interval of $\pm 2\sigma$ (95% rule) and approximating, we obtain the following expression for the maximum achievable swath width W_S, which looks, but for a square root, very similar to (14):

$$W_S \cong \left(1 - \frac{4}{\sqrt{3}} A\sqrt{n_t}\right) W_{S_{\mathrm{const}}} \approx (1 - 2A\sqrt{n_t}) W_{S_{\mathrm{const}}}. \quad (15)$$

The comparison of (15) and (14) highlights that, for a random PRI variation, the same swath reduction is obtained for a much larger PRI span (i.e., four times larger for $n_t = 16$) compared to the sinusoidal and square wave cases. While, for sinusoidal and square wave PRI variations, in fact, the swath reduction is proportional to the number of traveling pulses n_t, for periodic random PRI variation, the swath reduction is approximately proportional to the square root of the number of traveling pulses. This is shown with an example in Fig. 6, which refers to a TanDEM-X-like system characterized by a pulsewidth of 25 μs and a mean PRI $\mathrm{PRI}_{\mathrm{mean}} = 0.303$ ms, corresponding to a mean PRF of 3300 Hz. For the sinusoidal and square wave PRI variations, the parameters $N = 100$ and $A = 0.007$ have been used (resulting according to (14) to an

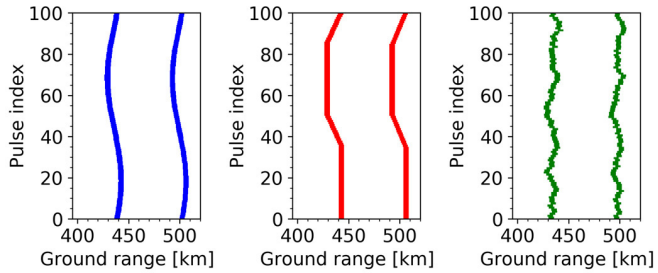

Fig. 6. Swath decrease at a slant range around $R_0 = 700$ km as a result of (left) sinusoidal PRI variation in (11) with $N = 100$ and $A = 0.007$, (center) square wave PRI variation of (12) with $N = 100$ and $A = 0.007$, and (right) random PRI variation of (13) with $N = 100$ and $A = 0.007(n)_t^{1/2} = 0.028$. The swath reduction is in all cases less than 14 km.

approximate swath reduction of about 22.4%), while, for the periodic random PRI variation, the parameters $N = 100$ and $A = 0.007(n)_t^{1/2} = 0.028$ have been used, which results in the same swath reduction (less than 14 km in ground range). Note that the areas in blue/red/green include not only the blind ranges in the raw data but also areas characterized by reduced range resolution after pulse compression [28], [29].

A larger PRI span implies further smearing of azimuth ambiguities, which might help reduce the critical baseline, as discussed above. The interval has been chosen around $\pm 2\sigma$ and not larger because the length of the PRI sequence is limited and so is the number of realizations. This justifies repeating the same random sequence rather than having a very long one (requirements on the minimum sequence length will be discussed in Section III-C). An "unfortunate" realization, in fact, can just be discarded, as the system designer can choose the PRI variation to be adopted for the acquisition in advance.

If the length of the PRI sequence N is instead equal to the number of traveling pulses n_t (or to $n_t - 1$), larger PRI span (and, namely, amplitudes A) can be exploited without incurring in a significant swath reduction. For all three considered PRI variations, in fact, the moving sum will be constant for one of the two blind ranges delimiting the swath due to the fact that the addends of the moving sum stay the same and almost constant for the other one, where the moving sum includes $N - 1$ out of the N values. In this case, for all three considered PRI variations, the same PRI span leads to the same swath reduction, and the maximum achievable swath width W_S can be approximated as

$$W_S \cong (1 - A) W_{S_{\mathrm{const}}}. \quad (16)$$

In this case, in fact, the maximum relative variation of the blind range is $2A$ (i.e., the highest possible difference between two PRIs of the sequence), but the swath reduction is only due to one of the two blind ranges.

Fig. 7 shows an example of the case $N = n_t$ for the three considered PRI variations. It is apparent that the swath reduction is much smaller than in Fig. 6 although the PRI span is much larger ($A = 0.05$ versus $A = 0.007$). For $N = n_t - 1$, the moving sum is constant for the closer of the two blind ranges, and (16) still holds.

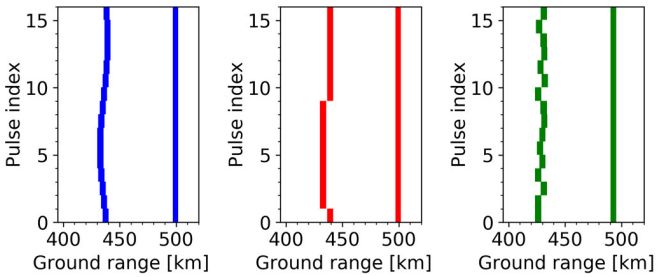

Fig. 7. Swath decrease for the case $N = n_t = 1$ at a slant range around $R_0 = 700$ km as a result of (left) sinusoidal PRI variation in (11), (center) square wave PRI variation of (12), and (right) random PRI variation of (13), all with $A = 0.05$. The swath reduction is in all cases less than 4 km.

C. Decorrelation and Along-Track Baseline

The PRI variation scheme and its parameters N and A have to be selected for a given along-track baseline in order to provide a substantial decorrelation of azimuth ambiguities while keeping the swath reduction as small as possible.

The trend of ambiguity decorrelation versus along-track baseline can be obtained for a specific set of system parameters and an along-track baseline by means of simulation. For a periodic PRI sequence, this trend will also be periodic with period $B_{a_{\text{period}}}$ given by

$$B_{a_{\text{period}}} = 2v_g \sum_{k=0}^{N-1} \text{PRI}_k \cong 2v_g N \text{PRI}_{\text{mean}}. \tag{17}$$

This means that, for an along-track baseline equal to integer multiples of $B_{a_{\text{period}}}$, the samples of master and slave in spite of the PRI variation and the nonzero along-track baseline will still be available at the same positions and will not determine any ambiguity decorrelation.

Given a sequence of PRI and an along-track baseline, it is possible to assess the resulting ambiguity decorrelation by convolving the impulse response of the ambiguity, which is, in general, different for the master and slave images, with fully developed speckle and estimating the coherence. For sinusoidal and square wave PRI variations, it can be observed that the coherence of the ambiguities decreases as the along-track baseline increases from 0 to $B_{a_{\text{period}}}/2$ (or from $pB_{a_{\text{period}}}$ to $pB_{a_{\text{period}}} + B_{a_{\text{period}}}/2$, with $p \in N$), as the relative shift between the available samples of master and slave increases. Likewise, as the along-track baseline increases from $B_{a_{\text{period}}}/2$ to $B_{a_{\text{period}}}$ (or from $pB_{a_{\text{period}}} + B_{a_{\text{period}}}/2$ to $(p+1)B_{a_{\text{period}}}$, with $p \in \mathbb{N}$), the coherence of the ambiguities increases. The maximum decorrelation, therefore, occurs for

$$B_a = (p + 1/2)B_{a_{\text{period}}}, \quad p \in \mathbb{N} \tag{18}$$

where $\mathbb{N}$ also includes 0. For random PRI variations, the along-track baseline that leads to the maximum ambiguity decorrelation depends on the specific PRI realizations; still, the minimum usually corresponds to the value of B_a given in (18).

These considerations, therefore, suggest that the length N of the PRI sequence can be selected (at least for sinusoidal and square wave schemes) so that the maximum decorrelation is obtained. By substituting (17) in (18), it holds

$$N \cong \frac{B_a}{2(p + 1/2)v_g \text{PRI}_{\text{mean}}}, \quad p \in \mathbb{N}. \tag{19}$$

The expression in (19) provides a set of possible values of N, which can be obtained by varying the integer variable p and, if needed, to some extent, the value of PRI_{mean}, assuming that B_a and v_g are given. For $B_a = 290$ m, $v_g = 7040$ m/s, and $\text{PRI}_{\text{mean}} = 0.303$ ms, for instance, we can choose $N = 136$ (corresponding to $p = 0$ and belonging to the case $N \gg n_t$) but also $N = 16$ (corresponding to $p = 4$ and belonging to the case $N = n_t$) or other further values of N.

Once different options for the sequence length are available, the parameter A, related to the PRI span, needs to be selected. In general, the higher the PRI span, the more substantial the ambiguity decorrelation, but also the more significant the swath reduction.

2-D simulations have been carried out for a typical spaceborne scenario and the same sequences for which the swath reduction had been assessed in Figs. 6 and 7. The coherence has been estimated using a 9×9 pixel window. Fig. 8 shows, for the aforementioned PRI variations, the coherence of the ambiguities as a function of the along-track baseline. These plots have to be considered periodical, i.e., they repeat with

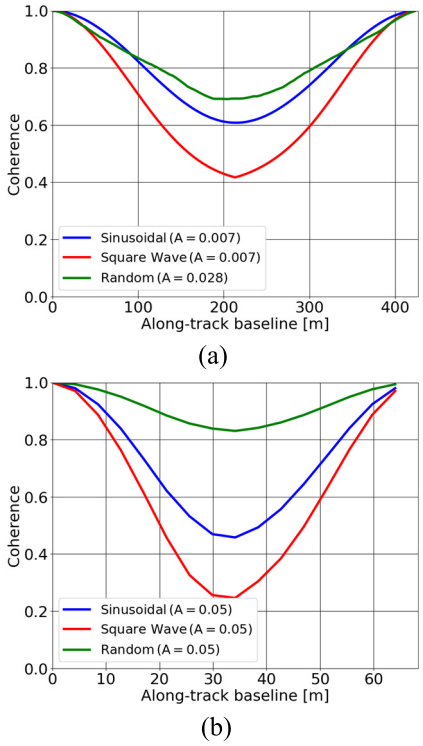

Fig. 8. Coherence of the ambiguities as a function of the along-track baseline for the sinusoidal PRI variation in (11) (blue), the square wave PRI variation of (12) (red), and the random PRI variation of (13) (green). (a) $N = 100$ (length of the sequence of PRIs is much larger than the number of traveling pulses) corresponding to swath width reduction depicted in Fig. 6. (b) $N = 16$ sinusoidal PRI variation (length of the sequence of PRIs equal to the number of traveling pulses) corresponding to swath width reduction depicted in Fig. 7.

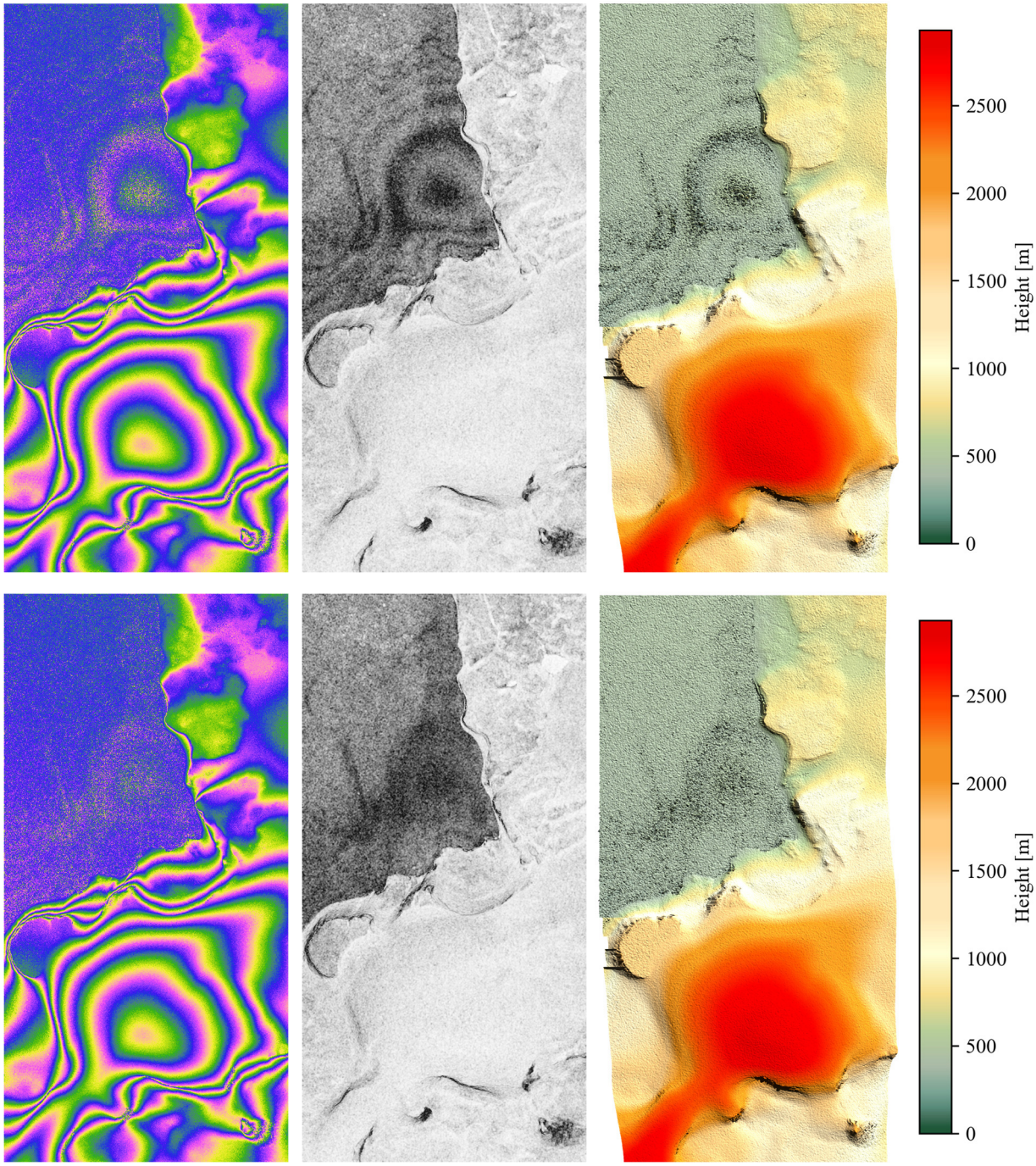

Fig. 9. Impact of (left) ambiguity decorrelation on interferometric phase, (center) magnitude of the complex coherence, and (right) DEM for AASR $= -17$ dB. (top) No decorrelation. (Bottom) Coherence of the ambiguity $= 0.3$. The horizontal and vertical axes represent the ground range (5.12 km) and the azimuth (10.24 km), respectively.

a period given by the maximum along-track baseline given in the plot.

It can be noticed that long sequences allow decorrelation for larger along-track baselines although one could also exploit, in some cases, the periodical effect with short sequences. As is apparent, for comparable swath reduction, the square wave PRI variation allows, in both cases, for the highest decorrelation, while a random PRI variation is less effective, especially if the length of the sequence of PRIs is equal to the number of traveling pulses. From Fig. 8(b), it can also be noticed that, in this example, which refers to the TanDEM-X system, substantial ambiguity decorrelation can be achieved, as long as the along-track baseline is larger than 20 m.

It is worth noticing that the minimum and maximum PRIs of the square wave variations of Figs. 6 and 7 correspond to differences in the instantaneous PRFs in the order of 55 and 330 Hz, respectively. This means that, in order to achieve a significant decorrelation of azimuth ambiguities in the

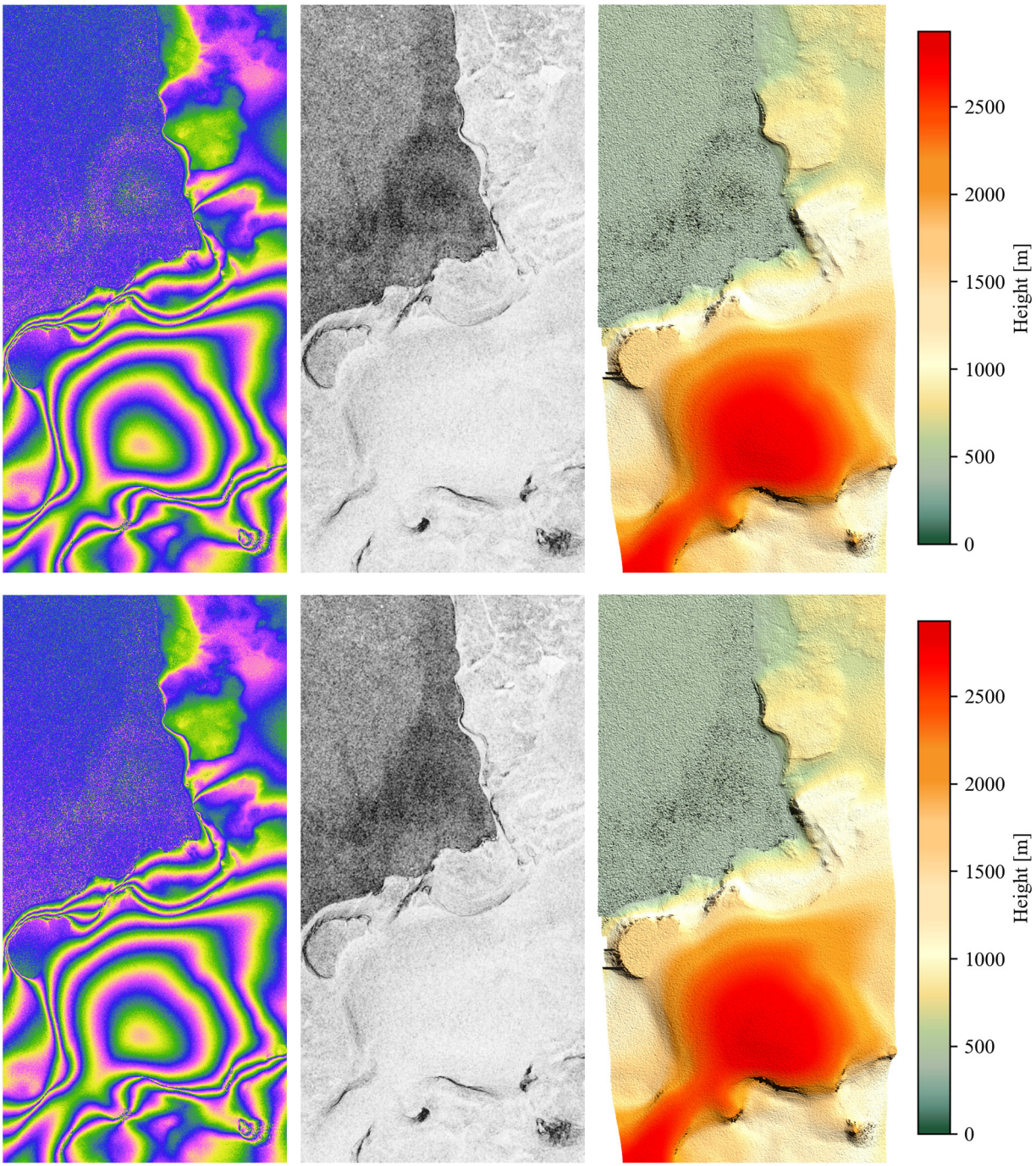

Fig. 10. Impact of (left) ambiguity decorrelation on interferometric phase, (center) magnitude of the complex coherence, and (right) DEM for AASR $= -22$ dB. (Top) No decorrelation. (Bottom) Coherence of the ambiguity $= 0.3$. The horizontal and vertical axes represent the ground range (5.12 km) and azimuth (10.24 km), respectively.

single-pass case, an instantaneous PRF change much larger than the PRF difference required for the repeat-pass case (only 8 Hz in the example of Section II) is needed.

At the end of Section II, it was observed that the PRF difference also determines a relative shift of range ambiguities. In the single-pass case, as a consequence of the continuous PRI variation, range ambiguous echoes appear at different ranges for each pulse, i.e., they spread over several range resolution cells and are also likely to be decorrelated [29].

IV. Impact on Interferogram and DEM Quality

In order to assess the impact of ambiguity decorrelation on interferogram and DEM quality, simulations are performed starting from the dataset of Fig. 1.

After having removed azimuth ambiguities from both the master and slave images using a Wiener filter (which provides an ambiguity suppression relative to the main signal suppression of about 11 dB), ambiguities have been artificially reintroduced in both the master and slave images by

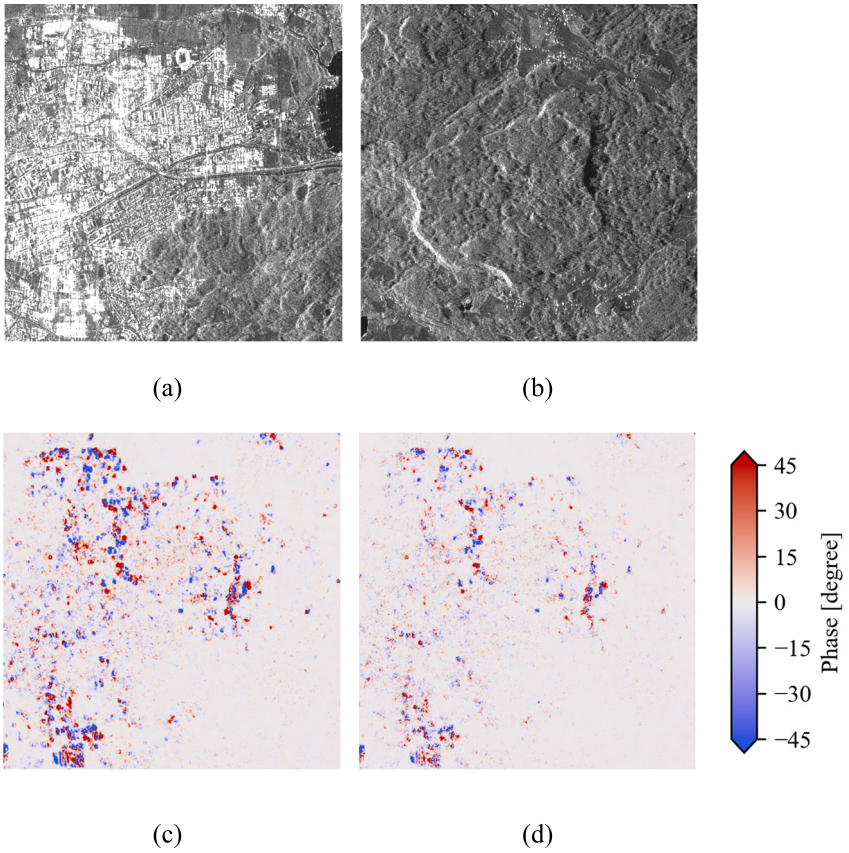

Fig. 11. Example of the impact of ambiguitydecorrelation on a land scene using a TanDEM-X dataset acquired near Klagenfurt am Wörthersee. (a) Portion of the SAR image (amplitude) responsible for azimuth ambiguities. (b) Portion of the SAR image (amplitude) affected by azimuth ambiguities. (c) Phase bias in the area affected by ambiguities in the case of no decorrelation. (d) Phase bias in the area affected by ambiguities in the case of ambiguity decorrelation equal to 0.3. The horizontal and vertical axes represent the ground range (4.93 km) and azimuth (4.11 km), respectively.

convolving the focused image with the IRF of the focused first-order azimuth ambiguity, translating it, and scaling it according to the desired ambiguity-to-signal ratio. Furthermore, ambiguity decorrelation has been introduced by multiplying the interferogram of the ambiguities by a phase screen generated according to the statistical distribution corresponding to the desired decorrelation level [1].

Figs. 9 and 10 show the resulting interferometric phase, the magnitude of the complex coherence, and the DEM obtained after phase unwrapping, for systems with AASR $=$ -17 dB and AASR $=$ -22 dB, respectively. Both the case of no decorrelation and that of coherence of the interferogram of ambiguities equal to 0.3, i.e., corresponding to almost complete ambiguity decorrelation, have been considered.

Fig. 9 corresponds to an AASR $=$ -17 dB and shows that, in the absence of ambiguity decorrelation, strong circular artifacts appear in both the interferometric phase and in the DEM. The same artifacts appear as a slight noise-like disturbance for the same AASR level and decorrelated ambiguities. The visual comparison of Figs. 9 (bottom) and 10 (top) also shows that the disturbance pattern obtained for AASR $=$ -17 dB and decorrelated ambiguities is very similar to that obtained for AASR $=$ -22 dB and coherent ambiguities, which confirms that decorrelating azimuth ambiguities through slight PRI variation represents a viable alternative to support demanding AASR requirements.

Whereas coherent effects of azimuth ambiguities are more apparent in low backscatter areas, such as water or sea ice, phase bias can also be noticeable and lead to nonnegligible height biases over land scenes. Fig. 11 shows a further simulation using a TanDEM-X dataset acquired near Klagenfurt am Wörthersee, Austria, and assuming AASR $=$ -17 dB. The portions of the SAR image responsible for and affected by azimuth ambiguities are shown in Fig. 11(a) and (b), respectively. The phase bias in the area affected by ambiguities in the case of no decorrelation and that of an ambiguity decorrelation equal to 0.3, i.e., corresponding to almost complete ambiguity decorrelation, is displayed in Fig. 11(c) and (d), respectively. In this example, the ambiguity decorrelation leads to a decrease in the average absolute phase bias from 7.1° to 4.6°, corresponding to a decrease in the average absolute height bias from 91 to 58 cm.

V. Conclusion and Outlook

This article tackles the problem of artifacts appearing in SAR interferograms as a result of the coherent interference of azimuth ambiguities and proposes a solution based on ambiguity decorrelation, which can be used as an alternative to or even in combination with other postprocessing techniques.

For the repeat-pass case, it is shown that it is enough to use two slightly different PRFs for the two acquisitions to decorrelate azimuth ambiguities. An analytical expression is provided for the minimum required PRF difference, which amounts to only few Hz for TanDEM-X. It is also mentioned that this PRF difference additionally shifts range ambiguities and, therefore, prevents possible coherence interference effects.

For the single-pass case, a slight variation of the PRI during the acquisition helps decorrelating ambiguities if an along-track baseline is present. For TanDEM-X, an along-track baseline larger than 20 m is required to achieve substantial ambiguity decorrelation. In particular, it is shown that the square wave PRI variation, i.e., repeating $N/2$ times a given PRI, then $N/2$ times a second PRI, then again $N/2$ times the first PRI, and so on, performs best. The square wave PRI variation is also the easiest to implement in most systems, e.g., it is the only one that can be straightforwardly implemented in TanDEM-X, as it does not require an extremely fine PRI variation. The PRI variation scheme needs to account for the along-track baseline of the acquisition and to be optimized accordingly. It could be investigated whether waveform diversity in addition to PRI variation could help achieve further ambiguity decorrelation.

While an accurate performance assessment can only be made for a specific system, simple simulations under conservative assumptions show the effectiveness of the technique, which could be useful for the design of future spaceborne interferometric SAR systems, such as High Resolution Wide Swath (HRWS) [36], as well as for the enhanced exploitation of current ones.

REFERENCES

[1] R. Bamler and P. Hartl, "Synthetic aperture radar interferometry," *Inverse Problems*, vol. 14, no. 4, pp. R1–R54, Aug. 1998.

[2] P. A. Rosen et al., "Synthetic aperture radar interferometry," *Proc. IEEE*, vol. 88, no. 3, pp. 333–382, Mar. 2000.

[3] R. F. Hanssen, *Radar Interferometry: Data Interpretation and Error Analysis*. Dordrecht, The Netherlands: Springer, 2001.

[4] A. Moreira, P. Prats-Iraola, M. Younis, G. Krieger, and I. P. K. Hajnsek, "A tutorial on synthetic aperture radar," *IEEE Geosci. Remote Sens. Mag.*, vol. 1, no. 1, pp. 6–43, Mar. 2013.

[5] H. A. Zebker and J. Villasenor, "Decorrelation in interferometric radar echoes," *IEEE Trans. Geosci. Remote Sens.*, vol. 30, no. 5, pp. 950–959, Sep. 1992.

[6] G. Krieger et al., "TanDEM-X: A satellite formation for high-resolution SAR interferometry," *IEEE Trans. Geosci. Remote Sens.*, vol. 45, no. 11, pp. 3317–3341, Nov. 2007.

[7] D. Massonnet, "Capabilities and limitations of the interferometric cartwheel," *IEEE Trans. Geosci. Remote Sens.*, vol. 39, no. 3, pp. 506–520, Mar. 2001.

[8] R. Fjortoft, J.-C. Souyris, J.-M. Gaudin, P. Durand, and D. Massonnet, "Impact of ambiguities in multistatic SAR: Some specificities of an L-band interferometric cartwheel," in *Proc. IEEE Int. Geosci. Remote Sens. Symp. (IGARSS)*, vol. 3, Sep. 2004, pp. 1754–1757.

[9] M. Villano and G. Krieger, "Impact of azimuth ambiguities on interferometric performance," *IEEE Geosci. Remote Sens. Lett.*, vol. 9, no. 5, pp. 896–900, Sep. 2012.

[10] M. Villano and G. Krieger, "Spectral-based estimation of the local azimuth ambiguity-to-signal ratio in SAR images," *IEEE Trans. Geosci. Remote Sens.*, vol. 52, no. 5, pp. 2304–2313, May 2014.

[11] M. Villano and G. Krieger, "Accounting for azimuth ambiguities in interferometric performance analysis," in *Proc. IEEE Int. Geosci. Remote Sens. Symp.*, Jul. 2012, pp. 299–302.

[12] A. Moreira, "Suppressing the azimuth ambiguities in synthetic aperture radar images," *IEEE Trans. Geosci. Remote Sens.*, vol. 31, no. 4, pp. 885–895, Jul. 1993.

[13] A. M. Guarnieri, "Adaptive removal of azimuth ambiguities in SAR images," *IEEE Trans. Geosci. Remote Sens.*, vol. 43, no. 3, pp. 625–633, Mar. 2005.

[14] Z. Yu and M. Liu, "Suppressing azimuth ambiguity in spaceborne SAR images based on compressed sensing," *Sci. China Inf. Sci.*, vol. 55, no. 8, pp. 1830–1837, Aug. 2012.

[15] M. Liu, Z. Yu, and C. Li, "Azimuth ambiguity suppression for spaceborne SAR based on PRF micro-variation," in *Proc. IEEE Int. Geosci. Remote Sens. Symp. (IGARSS)*, Jul. 2013, pp. 1325–1328.

[16] J. Chen, M. Iqbal, W. Yang, P.-B. Wang, and B. Sun, "Mitigation of azimuth ambiguities in spaceborne stripmap SAR images using selective restoration," *IEEE Trans. Geosci. Remote Sens.*, vol. 52, no. 7, pp. 4038–4045, Jul. 2014.

[17] G. D. Martino, A. Iodice, D. Riccio, and G. Ruello, "Filtering of azimuth ambiguity in stripmap synthetic aperture radar images," *IEEE J. Sel. Topics Appl. Earth Observ. Remote Sens.*, vol. 7, no. 9, pp. 3967–3978, Sep. 2014.

[18] J. Chen, K. Wang, W. Yang, and W. Liu, "Accurate reconstruction and suppression for azimuth ambiguities in spaceborne stripmap SAR images," *IEEE Geosci. Remote Sens. Lett.*, vol. 14, no. 1, pp. 102–106, Jan. 2016.

[19] Y. Long, F. Zhao, M. Zheng, G. Jin, and H. Zhang, "An azimuth ambiguity suppression method based on local azimuth ambiguity-to-signal ratio estimation," *IEEE Geosci. Remote Sens. Lett.*, vol. 17, no. 12, pp. 2075–2079, Dec. 2020.

[20] P. Lopez-Dekker, Y. Li, L. Iannini, P. Prats-Iraola, and M. Rodriguez-Cassola, "On azimuth ambiguities suppression for short-baseline along-track interferometry: The stereoid case," in *Proc. IEEE Int. Geosci. Remote Sens. Symp. (IGARSS)*, Jul. 2019, pp. 110–113.

[21] D. Richter, M. Rodriguez Cassola, M. Zonno, and P. Prats, "Coherent azimuth ambiguity suppression based on linear optimum filtering of short along-track baseline SAR interferograms," in *Proc. Eur. Conf. Synth. Aperture Radar (EUSAR)*, Leipzig, Germany, Jul. 2022, pp. 25–27.

[22] F. K. Li and W. T. K. Johnson, "Ambiguities in spaceborne synthetic aperture radar systems," *IEEE Trans. Aerosp. Electron. Syst.*, vol. AES-19, no. 3, pp. 389–397, May 1983.

[23] R. K. Raney and G. J. Princz, "Reconsideration of Azimuth Ambiguities in SAR," *IEEE Trans. Geosci. Remote Sens.*, vol. GE-25, no. 6, pp. 783–787, Nov. 1987.

[24] N. Ustalli and M. Villano, "Impact of ambiguity statistics on information retrieval for conventional and novel SAR modes," in *Proc. IEEE Radar Conf. (RadarConf)*, Sep. 2020, pp. 1–6.

[25] M. Villano, G. Krieger, and A. Moreira, "Nadir echo removal in synthetic aperture radar via waveform diversity and dual-focus postprocessing," *IEEE Geosci. Remote Sens. Lett.*, vol. 15, no. 5, pp. 719–723, May 2018.

[26] S.-Y. Jeon, T. Kraus, U. Steinbrecher, G. Krieger, and M. Villano, "Experimental demonstration of nadir echo removal in SAR using waveform diversity and dual-focus postprocessing," *IEEE Geosci. Remote Sens. Lett.*, vol. 19, pp. 1–5, 2022, doi: 10.1109/LGRS.2021.3095566.

[27] M. Villano, G. Krieger, and A. Moreira, "Staggered SAR: High-resolution wide-swath imaging by continuous PRI variation," *IEEE Trans. Geosci. Remote Sens.*, vol. 52, no. 7, pp. 4462–4479, Jul. 2014.

[28] M. Villano, G. Krieger, and A. Moreira, "A novel processing strategy for staggered SAR," *IEEE Geosci. Remote Sens. Lett.*, vol. 11, no. 11, pp. 1891–1895, Nov. 2014.

[29] M. Villano, "Staggered synthetic aperture radar," M.S. thesis, Karlsruhe Inst. Technol., Wessling, Germany, 2016.

[30] M. Villano, G. Krieger, M. Jäger, and A. Moreira, "Staggered SAR: Performance analysis and experiments with real data," *IEEE Trans. Geosci. Remote Sens.*, vol. 55, no. 11, pp. 6617–6638, Nov. 2017.

[31] M. Villano and M. N. Peixoto, "Characterization of nadir echoes in multiple-elevation-beam SAR with constant and variable pulse repetition interval," *IEEE Trans. Geosci. Remote Sens.*, vol. 60, pp. 1–9, 2022.

[32] M. Villano, M. N. Peixoto, N. Ustalli, G. Krieger, and A. Moreira, "Staggered SAR: Recent advances and design trade-offs," in *Proc. Eur. Conf. Synth. Aperture Radar (EUSAR)*, Leipzig, Germany, Apr. 2021, pp. 1–6.

[33] M. Pinheiro, P. Prats-Iraola, M. Rodriguez-Cassola, and M. Villano, "Analysis of low-oversampled staggered SAR data," *IEEE J. Sel. Topics Appl. Earth Observ. Remote Sens.*, vol. 13, pp. 241–255, 2020.

[34] M. Pinheiro et al., "Processing and performance analysis of NASA-ISRO SAR (NISAR) staggered data," in *Proc. IEEE Int. Geosci. Remote Sens. Symp. (IGARSS)*, Jul. 2019, pp. 8374–8377.
[35] H. A. Zebker, "A signal model for PRF dithering in wide-swath, fine-resolution InSAR," *IEEE Geosci. Remote Sens. Lett.*, vol. 18, no. 7, pp. 1214–1218, Jul. 2021.
[36] J. Mittermayer et al., "MirrorSAR: An HRWS add-on for single-pass multi-baseline SAR interferometry," *IEEE Trans. Geosci. Remote Sens.*, vol. 60, pp. 1–18, 2022.

Michelangelo Villano (Senior Member, IEEE) received the B.Sc. and M.Sc. degrees (Hons.) in telecommunication engineering from the Sapienza University of Rome, Rome, Italy, in 2006 and 2008, respectively, and the Ph.D. degree (Hons.) in electrical engineering and information technology from the Karlsruhe Institute of Technology, Karlsruhe, Germany, in 2016.

From 2008 to 2009, he was a Young Graduate Trainee with the European Space Research and Technology Center, European Space Agency, Noordwijk, The Netherlands, where he developed processing algorithms for ice-sounding radar. In 2017, he was a Visiting Research Scientist with the Communications, Tracking, and Radar Division, NASA Jet Propulsion Laboratory, Pasadena, CA, USA, where he analyzed novel acquisition modes for the NASA Indian Space Research Organization synthetic aperture radar (SAR) instrument. Since 2009, he has been with the Microwaves and Radar Institute, German Aerospace Center (DLR), Weßling, Germany, where he is currently the Head of the NewSpace SAR Research Group. Since 2019, he has been a Lecturer with Ulm University, Ulm, Germany. He has authored or coauthored over 110 research articles in peer-reviewed journals and international conference proceedings. He holds ten patents in the field of SAR. His research interests include the conception of innovative SAR modes for high-resolution wide-swath imaging and the development of low-cost SAR solutions for frequent and enhanced Earth monitoring.

Dr. Villano has been a member of the Technical Program Committee of the European Conference on SAR (EUSAR) since 2016. He was a recipient of the First Place Student Paper Award at the EUSAR, Berlin, Germany, in 2014, the IEEE Geoscience and Remote Sensing Society Letters Prize Paper Awards in 2015 and 2017, the Student Paper Award at the Asia–Pacific Conference on Synthetic Aperture Radar, Marina Bay Sands, Singapore, in 2015, the DLR Science Award in 2016, the Award as Young Scientist of the Foundation Werner von Siemens Ring in 2017, the ITG Dissertation Award in 2017, and the Best Paper Award at the German Microwave Conference 2019. In 2022, he was awarded a Starting Grant by the European Research Council. He is the Co-Chair of the Working Group on Remote Sensing Instrument and Technologies for Small Satellites of the IEEE Geoscience and Remote Sensing Society's Technical Committee on Instrumentation and Future Technologies. He has served as a Guest Editor for the special issues: Advances in Antenna Array Processing for Radar 2014 and Advances in Antenna Array Processing for Radar 2016 of the *International Journal of Antennas and Propagation*. He serves as an Associate Editor for the IEEE GEOSCIENCE AND REMOTE SENSING LETTERS.

Maxwell Nogueira Peixoto was born in Feira de Santana, Brazil, in 1996. He received the B.S. degree in electronic engineering and the M.S. degree in telecommunications from the Aeronautics Institute of Technology (ITA), São José dos Campos, Brazil, in 2020 and 2021, respectively. He is currently pursuing the Ph.D. degree in electronic engineering with Ulm University, Ulm, Germany.

In 2019, he was an Intern with the Microwaves and Radar Institute, German Aerospace Center (DLR), Weßling, Germany, where he worked at the NewSpace SAR Research Group on the topic of nadir echo characterization and suppression in staggered synthetic aperture radar (SAR). In 2021, he returned to the NewSpace SAR Research Group, Microwaves and Radar Institute, DLR, where he is currently researching the topic of distributed SAR interferometry using clusters of SmallSats. His research interests include radar signal processing, staggered SAR, and multi-baseline SAR interferometry.

Mr. Peixoto was a recipient of the Young Scientist Award at the Kleinheubacher Tagung 2021, Miltenberg, Germany.

Nertjana Ustalli (Member, IEEE) received the M.Sc. degree (Hons.) in communication engineering and the Ph.D. degree (Hons.) in radar and remote sensing from the Sapienza University of Rome, Rome, Italy, in 2014 and 2018, respectively.

From July 2018 to June 2019, she was a Post-Doctoral Researcher with the Department of Information Engineering Electronics and Telecommunications (DIET), Sapienza University of Rome, where she worked on the development of detection and motion parameters estimation techniques for moving targets in forward scatter radar configuration. Since October 2019, she has been with the Microwaves and Radar Institute, German Aerospace Center (DLR), Weßling, Germany. Her research interests include the development of cost-effective synthetic aperture radar (SAR) for dedicated applications, the investigation of phase synchronization approaches for small-satellite SAR constellations, and the analysis of ambiguities in conventional and waveform-encoded SAR modes.

Dr. Ustalli was a recipient of the Best Student Paper Award at the 2017 International Conference on Radar Systems, the Best Paper Award at the 2018 International Radar Symposium, the Best Paper Award at the 2018 GTTI Workshop on Radar and Remote Sensing, the Best 2018 Ph.D. Theses in the field of Communication Technologies defended at an Italian university, and the Young Scientist Award at the 2022 Kleinheubacher Tagung organized by the International Union of Radio Science.

Josef Mittermayer received the Dipl.Ing. (M.Sc.) degree in electrical engineering from the Technical University of Munich, Munich, Germany, in 1995, the M.Sc. degree in space system engineering from the Delft University of Technology, Delft, The Netherlands, in 2004, and the Ph.D. degree from the University of Siegen, Siegen, Germany, in 2000.

Since 1994, he has been with the Microwaves and Radar Institute, German Aerospace Center (DLR), Weßling, Germany. From 2002 to 2008, he worked on the TerraSAR-X project. From 2004 to 2008, he held the TerraSAR-X Group Leader position. He was also the Project Manager of TerraSAR-X System Engineering and Calibration and was technically responsible for the TerraSAR-X commissioning phase. Currently, NewSpace and formations of small multistatic SAR satellites are the focuses of his work. Apart from numerous conference papers and patents in the field of SAR, he is the author or a coauthor of more than 20 peer-reviewed journal articles. His scientific and engineering work includes the fields of synthetic aperture radar (SAR) processing, SAR system engineering, and SAR mode development.

Dr. Mittermayer and his colleagues were recipients of the IEEE Geoscience and Remote Sensing Society Transactions Prize Paper Award for a paper on air and spaceborne stripmap and ScanSAR processing in 1996. He was a recipient of the DLR Science Award in 2001 for his work on spotlight-SAR processing. In 2011, he was awarded the DLR Forschungssemester for his contribution to the TerraSAR-X project.

Gerhard Krieger (Fellow, IEEE) received the Dipl.Ing. (M.S.) and Dr.Ing. (Ph.D.) (Hons.) degrees in electrical and communication engineering from the Technical University of Munich, Munich, Germany, in 1992 and 1999, respectively.

From 1992 to 1999, he was with the Ludwig Maximilian University of Munich, Munich, where he conducted multidisciplinary research on neuronal modeling and nonlinear information processing in biological and technical vision systems. Since 1999, he has been with the Microwaves and Radar Institute, German Aerospace Center (DLR), Weßling, Germany, where he started as a Research Associate developing signal processing algorithms for a novel forward-looking radar system employing digital beamforming on receive. From 2001 to 2007, he led the New SAR Missions Group that pioneered the development of advanced bistatic and multistatic radar systems, such as TanDEM-X, as well as innovative multichannel synthetic aperture radar (SAR) techniques and algorithms for high-resolution wide-swath SAR imaging. Since 2008, he has been the Head of the Radar Concepts Department that hosts about 40 scientists focusing on new SAR techniques, missions, and applications. He has been serving as a Mission Engineer for TanDEM-X, and he made also major contributions to the development of the Tandem-L mission concept, where he led the Phase-0 and Phase-A studies. Since 2019, he has been holding a professorship at the Friedrich-Alexander-Universität Erlangen-Nürnberg, Erlangen, Germany. He is the author or a coauthor of more than 100 peer-reviewed journal articles, nine invited book chapters, more than 400 conference papers, and more than 20 patents.

Prof. Krieger received several national and international awards, including two Best Paper Awards at the European Conference on Synthetic Aperture Radar, two Transactions Prize Paper Awards of the IEEE Geoscience and Remote Sensing Society, and the W. R. G. Baker Prize Paper Award from the IEEE Board of Directors. In 2014, he has served as the Technical Program Chair of the European Conference on Synthetic Aperture Radar and a Guest Editor for the IEEE JOURNAL OF SELECTED TOPICS IN APPLIED EARTH OBSERVATIONS AND REMOTE SENSING. He has been an Associate Editor of the IEEE TRANSACTIONS ON GEOSCIENCE AND REMOTE SENSING since 2012.

Alberto Moreira (Fellow, IEEE) received the B.S.E.E. and M.S.E.E. degrees from the Aeronautical Technological Institute (ITA), São José dos Campos, Brazil, in 1984 and 1986, respectively, and the Dr.Eng. (Ph.D.) degree (Hons.) from the Technical University of Munich, Munich, Germany, in 1993.

From 1996 to 2001, he was the Head of the SAR Technology Department, German Aerospace Center (DLR), Weßling, Germany. Under his leadership, the DLR airborne synthetic aperture radar (SAR) system has been upgraded to operate in innovative imaging modes, such as polarimetric SAR interferometry, tomography, and holography. Since 2001, he has been the Director of the Microwaves and Radar Institute, DLR, and a Full Professor of microwave remote sensing with the Karlsruhe Institute of Technology (KIT), Karlsruhe, Germany. His DLR's Institute contributes to several scientific programs and projects for spaceborne SAR missions, such as TerraSAR-X, TanDEM-X, Tandem-L, High Resolution Wide Swath (HRWS), SAR-Lupe, and SARah, as well as Kompsat-6, PAZ, Sentinel-1, BIOMASS, ROSE-L, Harmony, Sentinel-1NG, Envision, and VERITAS. The mission TanDEM-X, led by his institute, has generated a global, high-resolution digital elevation model of the Earth with unprecedented accuracy. He is an initiator and a principal investigator (PI) for this mission. From 2012 to 2018, he has served as a principal investigator of the Helmholtz Alliance "Remote Sensing and Earth System Dynamics" in support of Tandem-L. He has served as a member of the ESA Mission Advisory Groups of ENVISAT/ASAR, Sentinel-1, and Hydroterra, and is currently serving as a member of the Science Study Team for the ESA's mission EnVision. He is the author or a coauthor of more than 450 publications in international conferences and journals, and eight book chapters. He holds more than 40 international patent grants in the radar and antenna field. His professional interests and research areas encompass spaceborne radar end-to-end system design, microwave techniques and system concepts, signal processing, and remote sensing applications.

Prof. Moreira and his colleagues received the GRSS Transactions Prize Paper Awards in 1997, 2001, and 2007 and the GRSS Letters Prize Paper Awards in 2015 and 2017. He was a recipient of several international awards, including the IEEE AESS Nathanson Award in 1999, the IEEE Kiyo Tomiyasu Field Award in 2007, the IEEE W. R. G. Baker Award from the IEEE Board of Directors in 2012, the IEEE GRSS Distinguished Achievement Award in 2014, and the IEEE Dennis J. Picard Medal for Radar Technologies and Applications in 2023. He has served as the General Co-Chair of International Geoscience and Remote Sensing Symposium (IGARSS) in 2012. He has been serving as the Chair of the Major Awards of the GRS Society since 2017. He was the Founder and the Chair of the GRSS German Chapter from 2003 to 2008. He has served as an Associate Editor for the IEEE GEOSCIENCE AND REMOTE SENSING LETTERS from 2003 to 2007. He has been serving as an Associate Editor for the IEEE TGRS since 2005. He has served as the President of the IEEE Geoscience and Remote Sensing (GRS) Society in 2010.